

COMMON ENVELOPE LIGHT-CURVES – I. GRID-CODE MODULE CALIBRATION

PABLO GALAVIZ^{1,2}, ORSOLA DE MARCO^{1,2}, JEAN-CLAUDE PASSY^{3,*}, JAN E. STAFF^{1,2} ROBERTO IACONI^{1,2}*Draft version February 28, 2017*

ABSTRACT

The common envelope binary interaction occurs when a star transfers mass onto a companion that cannot fully accrete it. The interaction can lead to a merger of the two objects or to a close binary. The common envelope interaction is the gateway of all evolved compact binaries, all stellar mergers and likely many of the stellar transients witnessed to date. Common envelope simulations are needed to understand this interaction and to interpret stars and binaries thought to be the byproduct of this stage. At this time, simulations are unable to reproduce the few observational data available and several ideas have been put forward to address their shortcomings. The need for more definitive simulation validation is pressing, and is already being fulfilled by observations from time-domain surveys. In this article, we present an initial method and its implementation for post-processing grid-based common envelope simulations to produce the light-curve so as to compare simulations with upcoming observations. Here we implemented a zeroth order method to calculate the light emitted from common envelope hydrodynamic simulations carried out with the 3D hydrodynamic code Enzo used in unigrid mode. The code implements an approach for the computation of luminosity in both optically thick and optically thin regimes and is tested using the first 135 days of the common envelope simulation of Passy et al. (2012), where a $0.8 M_{\odot}$ red giant branch star interacts with a $0.6 M_{\odot}$ companion. This code is used to highlight two large obstacles that need to be overcome before realistic light curves can be calculated. We explain the nature of these problems and the attempted solutions and approximations in full detail to enable the next step to be identified and implemented. We also discuss our simulation in relation to recent data of transients identified as common envelope interactions.

Subject headings: Binaries: close – hydrodynamics – methods: numerical – radiation mechanisms: thermal – stars: evolution – stars: variables: general

1. INTRODUCTION

The common envelope (CE) interaction between two stars has become the standard explanation for the existence of close evolved binaries such as cataclysmic variables or the progenitors of Type Ia supernovae (?). Yet, this interaction continues to elude a reasonable physical description. Without it, it becomes difficult to carry out meaningful population synthesis studies (e.g., Politano & Weiler 2007; Politano et al. 2010; Dominik et al. 2012), including those allowing us to reconcile predicted and observed rates of gravitational-wave producing events (e.g., Dominik et al. 2012, 2015). Hydrodynamic models have been carried out with a range of codes (Rasio et al. 1996; Sandquist et al. 1998; Ricker & Taam 2012; Passy et al. 2012; Nandez et al. 2013; Ohlmann et al. 2016; Iaconi et al. 2017), but it appears that even the basics of the interaction, such as the final separation or how much and when the CE is ejected, are poorly reproduced by these models.

Comparing model outputs with observations has mainly been limited to post-CE systems (e.g., Schreiber & Gänsicke 2003; Zorotovic et al. 2010; De Marco et al. 2011). The separations of post-CE systems tend

to be larger in some simulations than in observations (De Marco et al. 2011; Passy et al. 2012; Iaconi et al. 2017), although it is clear that simulated primaries with more massive and/or more compact envelopes result in smaller orbital separations (Ohlmann et al. 2016; Iaconi et al. 2017).

The assumption is that post-CE systems are generated by the entire removal of the stellar envelope over one dynamic event. Most CE simulation do not succeed in ejecting the entire envelope (Sandquist et al. 1998; Ricker & Taam 2012; Passy et al. 2012; Staff et al. 2016; Iaconi et al. 2017). Recently, some simulations have successfully achieved envelope ejection by assuming that the entire recombination energy budget is available for the ejection (Nandez et al. 2015; Nandez & Ivanova 2016). Even so, successful ejection only takes place for certain parameters (Nandez & Ivanova 2016). Moreover, some recombination energy may escape, as the neutral medium becomes optically thin (Harpaz 1998). As a result of the discrepancies between simulations and observations it is non-trivial to use the observations as code validation (for a review of the CE problem see ?), as one may suspect additional physics or phases, not modelled in the simulations, may play a role (e.g., Kuruwita et al. 2016; Ivanova & Nandez 2016).

Recently, time-resolved observations have detected a range of new outbursts, which have been named intermediate luminosity optical transients (ILOT; Kasliwal 2012; Kashi et al. 2013), so called because they have intermediate luminosities between those of novae and supernovae and lead to extremely red outburst products.

Pablo.Galaviz@me.com

¹ Department of Physics and Astronomy, Macquarie University, Sydney, NSW, Australia² Astronomy, Astrophysics and Astrophotonics Research Centre, Macquarie University, Sydney, NSW, Australia³ Argelander-Institut für Astronomie, Auf dem Hügel 71, D-53121 Bonn, Germany

* Alexander-von-Humboldt fellow

Some of these ILOTs appear to have been due to the merger of two stars. In particular the V1309 Sco ILOT (Tylenda et al. 2011) has almost certainly been caused by the merger of a subgiant and a low mass companion, because the contact binary was actually observed before the outburst, the period was reducing, and the post-merger object, a large giant, shows no sign of binarity. Other such objects may have been V838 Mon (Bond et al. 2003), V4332 Sgr (Martini et al. 1999) as well as other, extragalactic ones such as M31 RV (Mould et al. 1990) or M85 OT2007 (Kulkarni et al. 2007) or M31 LRN2015 (MacLeod et al. 2016). These outbursts, may give us an early glimpse into the light properties of CEs and hence provide us with additional model constraints and code validation.

As data accumulates we are already glimpsing at the complexity of these phenomena. It is clear that there are various phases characterising these presumed mergers: a phase preceding the dynamical merger, the dynamical merger itself, and a phase following it, all of which have distinct light properties that contribute to the overall light behaviour (MacLeod et al. 2016). The possible processes that change a slowly evolving binary to a fast merging one are several, including the Darwin-instability (MacLeod et al. 2016) or a slower merger driven by mass loss through the outer Lagrangian point (Pejcha et al. 2016b,a). As observations and models multiply, the role of CE simulation becomes a less and less isolated one and different codes and methods will have to be merged, or at least laid alongside (for a review of the range of codes applied to these problems see De Marco & Izzard 2017).

In so doing CE codes will have to evolve to their next generation, with higher resolution (Ohlmann et al. 2016) and the addition of extra physics, such as a more refined equation of state (Nandez et al. 2015) or the addition of magnetic fields (Ohlmann et al. 2016). In particular, radiation hydrodynamics will be a fundamental component in understanding the light expected from the CE fast inspiral phase. This step will allow us to understand when a CE takes place and when other emission systems are dominating the light.

In this paper we attempt the calculation of the light properties of one simulation of the CE early fast-in-spiral phase by post-processing one of the hydrodynamic simulations of Passy et al. (2012), hereafter P12. The challenges presented by the CE binary interaction when attempting to extract the light properties from simulations are even greater than those encountered when trying to determine the gas dynamics. However these challenges need to be quantified in order to improve the calculation to the point of being useful. Quantifying the challenges to the accurate calculation of a CE light curve can also focus future hydrodynamic efforts towards aspect of the computation that can aid the post-processing of the light.

The paper is organised as follows: in Section 2 we describe the physical situation of the early in-spiral of the CE interaction between a giant and a less massive companion. In so doing we set the stage and introduce some of the challenges. In Section 3 we summarise the luminosity calculation approach, with details left to the appendix, where we emphasize the challenge of knowing the photospheric temperature. This is followed by the calculation of the lightcurve for the CE simulations presented by P12 in Section 4. We then discuss available

observational constraints in Section 5. Conclusions and discussions are presented in Section 6.

2. THE PHYSICAL SITUATION

Before attempting the calculation of the light, it is important to define the physical regime and the parameters of the calculation. The simulation we base this work on is *Enzo2* of P12, carried out between a $0.88 M_{\odot}$, $89 R_{\odot}$, RGB star and a $0.6 M_{\odot}$, point mass companion. Their simulation was carried out using a domain size of 2 AU and 128 cells on a side⁵. Here we have repeated the simulation using the same code and setup, but with a domain four times as large and a 512 cells on a side so as to maintain the resolution identical (the cell size is $3.4 R_{\odot}$). The reason for this was to prolong the time during which the CE gas remains in the computational domain.

In Fig. 1 we show a slice along the equatorial plane at three times during the simulation, at the beginning, right after the one-dimensional (1D) stellar structure has been mapped and stabilised, at 75 days and at 135 days. We display density, temperature, velocity modulus, the ratio of gas to radiation pressure and the Mach number. In Fig. 2 we show a zoomed in detail of some of these quantities. Here we can also see the discrete nature of the grid and its relatively low resolution.

In Fig. 3 we show 1D cuts at time zero where we can see the problem of mapping a higher resolution, 1D stellar structure onto a three-dimensional (3D) computational domain with far inferior resolution. The photosphere, as defined by the 1D model, has values of pressure, temperature, density, etc. which are vastly different from those encountered near the centre of the star. These changes are well captured by the 1D model, but lost as soon as it is interpolated onto the 3D domain. This is why in Fig. 3 even the 1D model (red curves) is missing the points associated with the cooler, low density, photospheric layers: they are all contained within one cell of the 3D domain.

In Fig. 4 we show an important aspect of the convective giant star that will become important at a later time, when we face the problem of the photospheric temperature. The luminosity of each layer in a radiative, spherical star is always equal to:

$$L(r) = -4\pi r^2 \frac{c}{3\kappa(r)\rho(r)} \frac{\partial u_{\text{rad}}(r)}{\partial r}, \quad (1)$$

where r is the radius, c the speed of light, κ the opacity, ρ the density and u_{rad} is the radiative energy density. This is not so for the convective layers where it is the bulk motion of the convective eddies or plumes that transports out the energy. Hence, applying the above expression to our 1D model, we see how in the deep convective envelope the radiative luminosity is small, while it increases to the total value in the outer thin radiative layer.

In the 3D simulation the gas is adiabatic and this must be a reasonable approximation because of the short duration of the expansion. The only heating is at the hand of compression and some shock heating early in the simulation (Fig. 1). Some CE interactions do result in stronger shocks, but not all. In the interaction simulated by P12,

⁵ *Enzo2* was not the most resolved simulation of P12, but the outcome of this simulation were not too different from their *Enzo7* simulation, which had twice the resolution.

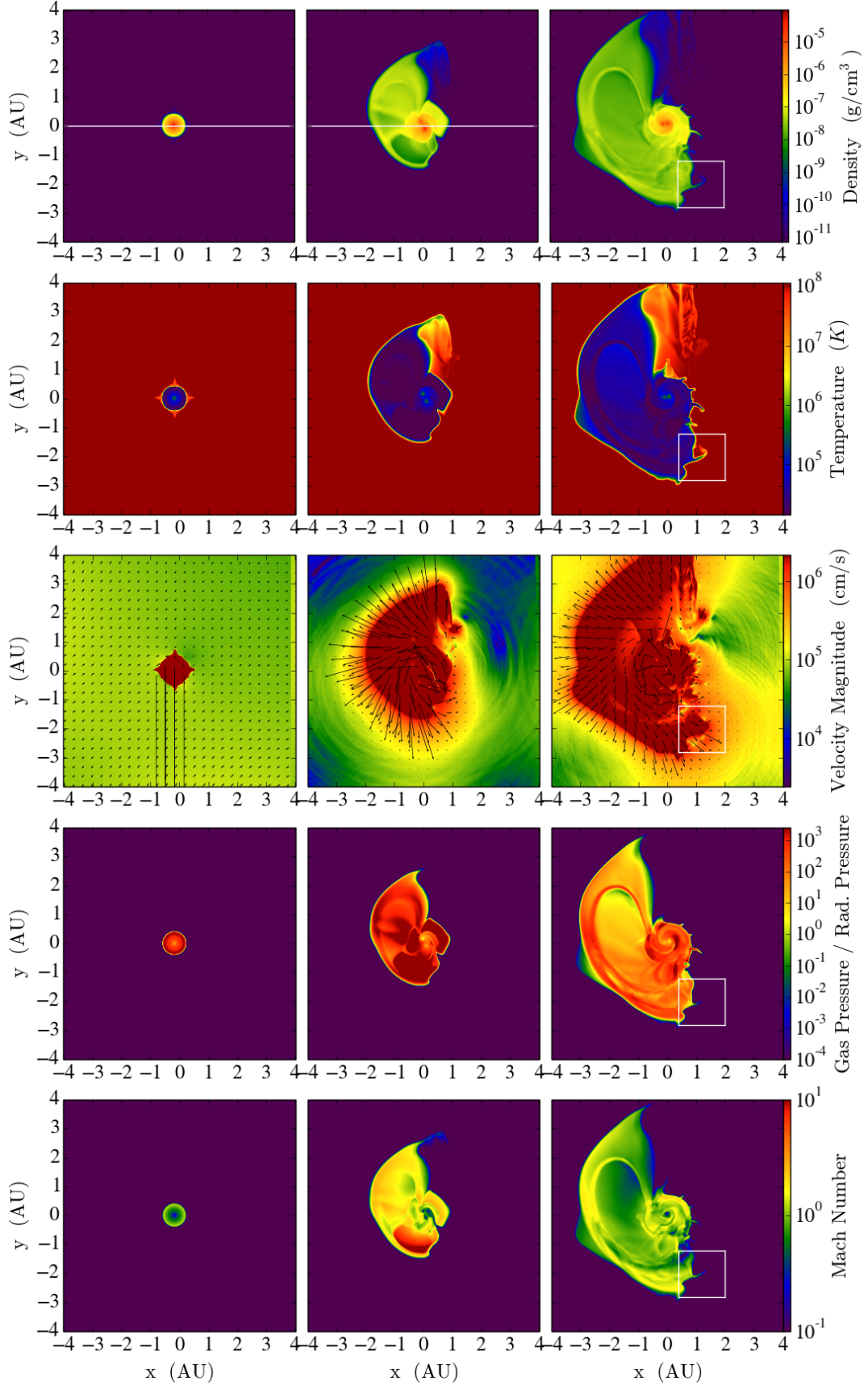


FIG. 1.— Slices on the equatorial plane of density (row 1), temperature (row 2), velocity of the gas (row 3), ratio between the gas pressure and the radiation pressure (row 4), and Mach number (row 5). The slices are for $t = 0$ (left column), $t = 75$ (middle column), and $t = 135$ days (right column). The arrows show the direction of the velocity and are normalised to the maximum value. In the vacuum, the ratio between the gas pressure and the radiation pressure is of the order 10^{-13} . The white box delimits the close-up region presented in Fig. 2. Horizontal white lines mark the direction of 1-dimensional cuts presented in future figures.

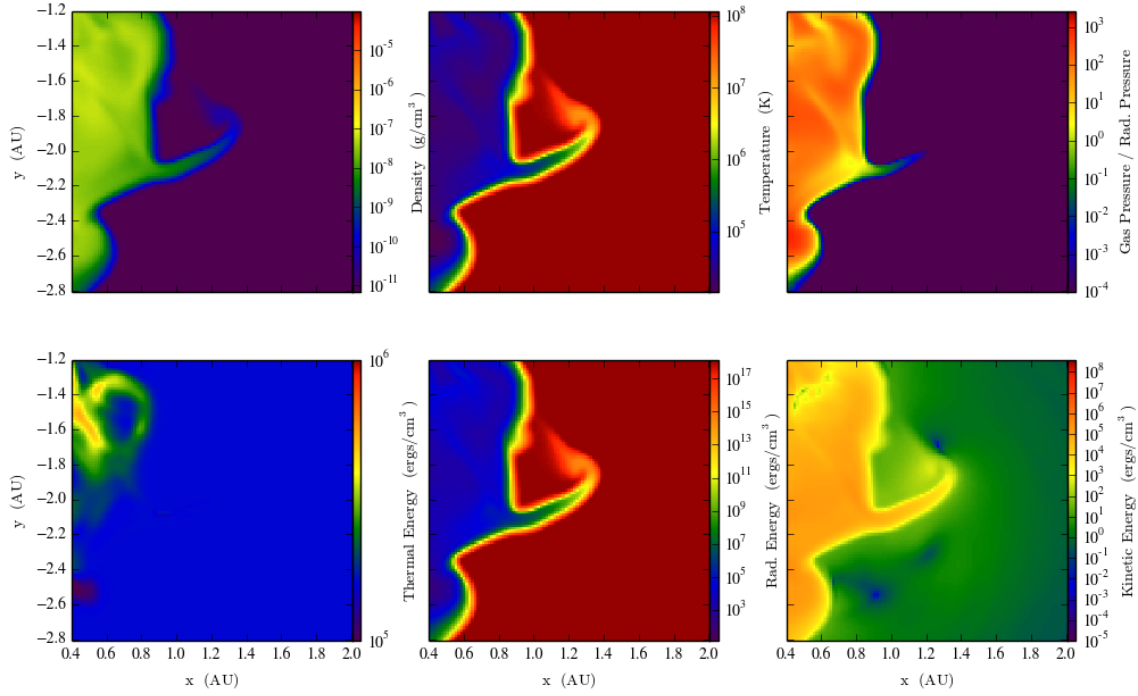


FIG. 2.— Details of slices on the equatorial plane of density (top left), temperature (top middle), gas pressure divided by radiation pressure (top right), thermal energy density (bottom left), radiation energy density (bottom middle) and kinetic energy density (bottom right), at $t = 135$ days from the beginning of the simulation. The centre of each panel is approximately at $x = 1.2$ AU and $y = -2$ AU from the centre of the domain (see Fig. 1).

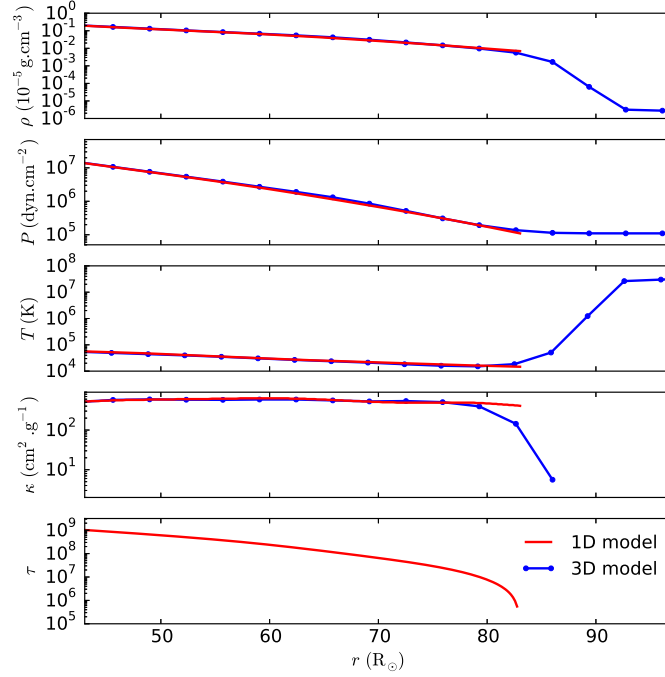


FIG. 3.— 1D (red lines) vs 3D (blue lines) comparison: the radial profile in 3D is a ray in the z direction which contains the origin. The different panels compare the interpolations of the density (row 1), the gas pressure (row 2), temperature (row 3), opacity (row 4), and optical depth (row 5).

the $0.6 M_{\odot}$ companion moves subsonically (Iaconi et al. 2017) although we do see locally mildly supersonic gas before 135 days.

The high temperature of the gas around the star (see the temperature panels in Fig. 1) is an artificial expedient commonly used in this type of grid computations (e.g., Sandquist et al. 1998). It insures that the stellar surface does not expand into the vacuum by providing a pressure that balances the atmospheric pressure by way of a very high temperature, but very low density “vacuum gas”. While this expedient has no consequence for the hydrodynamics, it is very problematic when extracting the light properties of the CE. As the simulation progresses, the outermost layers of the CE, which have lower densities, acquire a relatively large temperature as they “mix” with vacuum gas. These layers are dynamically unimportant, but they have an artificially high temperature and high opacity. These thin, hot layers can be seen clearly in the temperature panels in Fig. 1 and Fig. 2, even at time zero, where a yellow “skin” surrounds the the gas distribution.

Like these artificially hot layers, the low density “vacuum” is completely opaque. Any model that attempts to calculate the light from these simulations will have to devise a way to avoid the low density “vacuum” as well as any low density gas which has an unrealistically high temperature. As we explain below, we do this by imposing a “density floor”: gas with density lower than this floor is completely ignored in the calculation of the optical depth. In the detail in Fig. 2, top row, we see a small, low density, high temperature plume that is eliminated by the density floor.

In certain physical situations, such as supernova explosions, the relationship between gas thermal and radiation energies and expansion is such that photons can leak out from behind the photosphere. This is not the case here. A CE expansion during the dynamical in-spiral is a relatively slow process more akin to the expansion of a Mira giant during its radial pulsation cycle than the expansion of an envelope during a supernova eruption.

The early expansion phase which we are trying to characterise here is extremely optically thick, with almost none of the expanding gas becoming transparent. The speed at which the expansion takes place is of the order of tens of kilometres per second. In Fig. 1, third row, we see that the expansion early in the interaction is below 50 km s^{-1} with only few pockets of material moving faster (the maximum velocity witnessed in the first 135 days of the simulation is 200 km s^{-1}). The Mach number of the gas is just over unity by 135 days and decreasing, with the exception of a pocket of gas at 75 days, which eventually disappears. Over the entire simulation, gas pressure dominates over radiation pressure, except in the “vacuum” and within the thin skin of gas binding the envelope, that is heated by the external medium. The timescale of in-spiral is of the order of a year, with the expansion continuing beyond this time frame with a decreasing velocity.

Additionally, none of the energy associated with the in-spiral escapes during the short time of the in-spiral. As the companion in-spirals the gravitational energy is deposited into the gas in the form, primarily, of thermal energy and to a much lesser degree of kinetic energy of

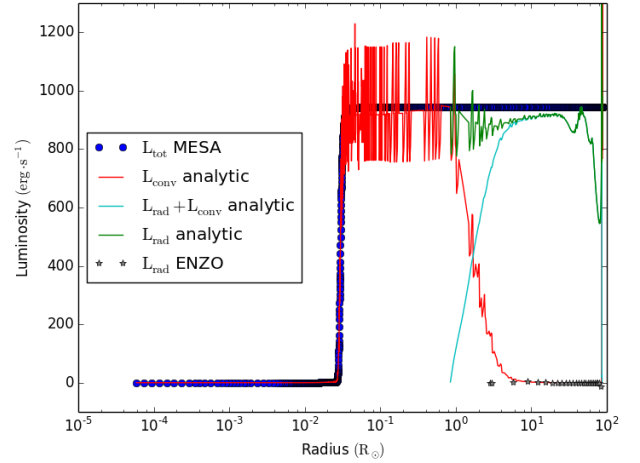


FIG. 4.— A comparison of the stellar luminosity as a function of radius calculated in 1D (blue symbols), compared with that derived from the analytical expression of Eq. 1 (red curve) and that calculated using the analytical expression after the star was mapped in 3D (green stars). The convective flux and luminosity was also calculated analytically (cyan line) and added to the radiative luminosity (red line) to make up total luminosity (green line).

the orbit as well as of the gas itself. The thermal energy will escape the star but on timescales longer than 135 days. In Fig. 5 we show the time photons would take to travel from a certain depth in the CE to the photosphere. This calculation is carried out by using a simple random walk theory with unequal step sizes (Mitalas & Sills 1992), and is demonstrated for different times during the CE interaction (0, 75 and 135 days). As we can see the time that the photons would take to travel out is always longer than the time over which we want to calculate the light-curve, namely 135 days. Hence in the first 135 days we do not expect any of the energy deposited into the CE by the in-spiralling companion to escape.

In Fig. 6 we display the values of temperature and density along a ray from the centre of the domain to the domain boundary along the positive x direction, at the usual three times during the simulation. The data points in the lower left corner of the plot, at low density and temperature are those located outside the photosphere, within the hot vacuum that is excluded in our simulation. Here we can see that all cells considered contain ionised gas ($T > 10000 \text{ K}$), so the dominating opacity source is from electron scattering.

3. LUMINOSITY CALCULATION AND THE TEMPERATURE PROBLEM

The CE Light Module (CELMO) reads the density and internal energy of each volume element in the 3D computational domain for each time step for which the hydrodynamic code has created an output. From the internal energy, a temperature is determined and, using the density and temperature, an opacity is interpolated using opacity tables. In opacity tables the opacities are expressed as a function of $\log T$ and $\log R$, where $R = \log \rho - 3 \log T + 18$. We have used opacity tables for $Z=0.02$ and $X=0.7$ from Grevesse & Sauval (1998) and Alexander & Ferguson (1994) with metals from Grevesse & Noels (1993). The latter table extends to temperatures as low as 1000 K (in the hydrodynamic simulations used in this paper, the

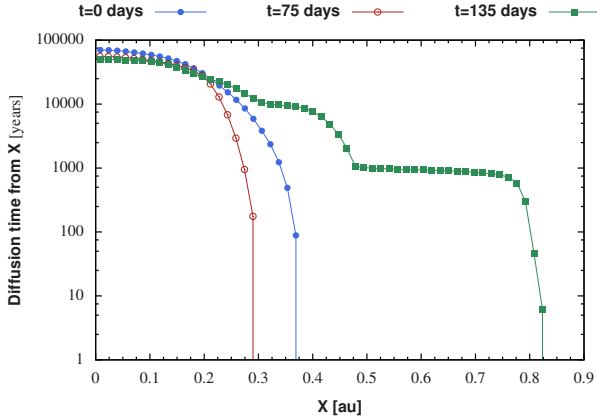


FIG. 5.— Diffusion time taken by a photon emitted at a distance x from the centre to reach the photosphere. The calculations are made for the gas configurations observed at $t = 0$ (blue), 75 (red), and 135 (green) days.

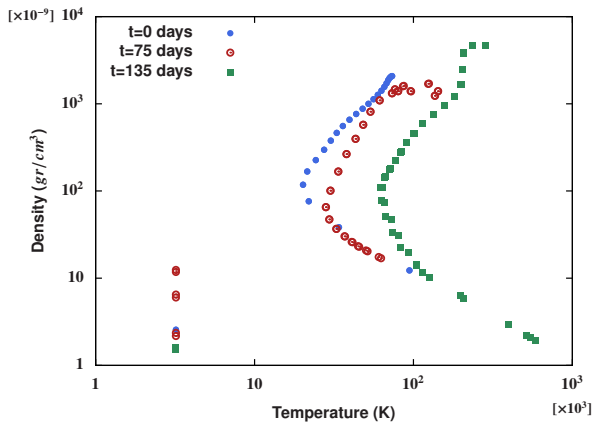


FIG. 6.— Density-temperature profiles at three times during the simulation.

temperature is never below this value). Using the density and the opacity, the optical depth is integrated for each volume element along parallel rays that are perpendicular to each face of the numerical domain. In this way the location of the surface where the optical depth is $2/3$, is found and the temperature of that location used (but see Section 3.1), assuming blackbody radiation, to determine the brightness of each volume element. In Appendix A we describe these steps in detail. In Appendix A.1 we describe the convolution with filter bandpasses, while in Appendix A we perform numerical tests to verify our implementation.

3.1. The calculation of temperature

When the 1D model is mapped into the ENZO computational domain, the temperature quantity is not required, since the specific internal energy of each cell, u_{int} , is calculated from the pressure and density. The ENZO equation of state is that of an ideal gas with an adiabatic index $\gamma = 5/3$, while the 1D star was calculated with a more sophisticated, depth-dependent equation of state. When the 1D star is mapped into the 3D domain it is not in perfect hydrostatic equilibrium. This is why, after the initial mapping, the star needs to be stabilised in ENZO, as described in P12. The new equilibrium model

tends to be slightly larger than the original 1D model.

This slightly larger star constitutes the initial model in ENZO, which we use for the initial calculation of the luminosity. Fig. 3 shows a typical comparison between the 1D model and the one used in the 3D model after relaxation, where we are zooming in onto the outer part of the star. Here the 1D model is missing the data points characterising the photosphere. These data points are all at almost the same radius, have very low density, contain almost no mass, but can create a problem when the star is immersed in the hot vacuum. The photosphere is therefore usually eliminated from the 1D model at the time of mapping it into 3D. Even if we had retained the 1D photosphere, the contact with the hot vacuum would, by the second time step, have heated these layers to an unrealistically high temperature, generating the problem which we discuss further below.

The temperature at each cell centre in the 3D code is given by:

$$T = \frac{M}{\bar{R}} (\gamma - 1) u_{\text{int}}, \quad (2)$$

where \bar{R} is the universal gas constant, $M = \mu m_H N_A$ is the molar mass, μ is the mean molecular weight, m_H is the hydrogen atomic mass and N_A is Avogadro's number. The temperature changes depending on the composition. The photospheric temperature for the simulation presented in Section 4 is smaller than 10 000 K, which is the approximate limit for a neutral gas. We therefore choose to use a mean molecular weight of 1.26, corresponding to neutral mass fractions of $X = 0.73$, $Y = 0.25$ and $Z = 0.02$.

3.2. The problem of spatial resolution in defining the effective temperature

The optical depth τ , determines the amount of radiation which is visible to an observer. The photosphere is located at a surface where $\tau = 2/3$ (approximately half of the radiation is visible). The volume of fluid above the photosphere defines the optical thickness of the fluid. We define two regimes in our simulation. We call optically thick every ray for which the back of the first cell occupied by gas with density above the CELMO density floor (first discussed at in Sec. 2 and better described in Sec. 3.3), has an optical depth larger than $2/3$.

For the optically thick fluid that characterise the early expansion of the CE, the $\tau = 2/3$ surface is located to the precision of the hydrodynamic code resolution. The greater problem is that the gradient of temperature within the cell that contains the photosphere is very steep. Consequently, while the physical location of the photosphere is affected by a modest uncertainty, the estimation of the effective temperature, and hence of the luminosity is far more inaccurate.

Within the cell that contains the photosphere, the optical depth ranges between zero at the “front” side of the cell, to a value much larger than unity, at the “back” side. The temperature at the centre of the same cell can have an arbitrarily high value because of the steep temperature gradient in the proximity of the stellar photosphere. A straight interpolation between the two cells in front and behind the cell containing the photosphere, is meaningless. The cell in front usually has a temperature value related to the “vacuum” temperature discussed in Sec. 2,

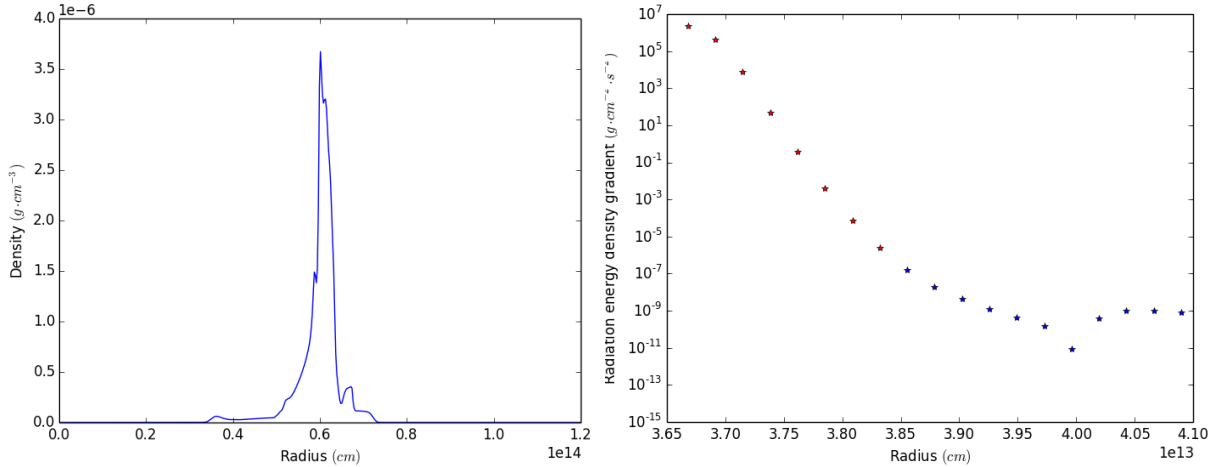


FIG. 7.— Left: A density cut at 75 days along the x-axis at $y=z=4$ AU (see ray plotted in Fig. 1). Right: the values of $\partial u_{\text{rad}}/\partial r$ at cell boundaries, centred on the left hand side of the density distribution at the location of the photosphere (blue symbols are inside the photosphere, while red symbols are outside).

hence unrealistically high. The temperature at the centre of the cell “behind” the cell containing the photosphere has the high value characteristic of a location farther inside the star. Hence finding the correct photospheric temperature is impossible by interpolation, because we have no knowledge of the external value. Using a value of zero, or similar low value for the cell just outside that containing the photosphere, and using one or even multiple points to interpolate the temperature at centre of the cell containing the photosphere, gives a range of possible values, which are dependent on arbitrary fit parameters. These fitting methods give an answer for the temperature to within a factor of 2, but the T^4 dependance of the luminosity makes these uncertainties unacceptable.

Below we discuss a second problem inherent to grid-based CE simulations that has an even worse impact on our attempt to calculate the light from the interaction.

3.3. The “vacuum” temperature problem

As explained in Sec. 2, in grid simulations the vacuum outside the star cannot be empty, because otherwise the star diffuses rapidly out (e.g., see Sandquist et al. 1998, P12). To obviate this problem the vacuum is replaced with a very low density medium. The density is a factor of 10^{-4} smaller than the lowest stellar density. In the case of the simulations presented in Section 4 the ENZO density floor is $7 \times 10^{-12} \text{ g cm}^{-3}$. The low density medium is kept in pressure equilibrium with the star surface by having a high temperature ($\sim 10^8 \text{ K}$).

Such high “vacuum” temperature would be optically thick, so CELMO has a minimum density below which the medium is considered completely optically thin. This “density floor” has to be larger than the density floor in the ENZO simulation for the following reason. At the beginning of the CE simulation low density, hydrodynamically unimportant “fingers” of stellar gas expand into the vacuum and their temperature is affected by the high “vacuum” temperature, so these low density features have unrealistically high temperature and are therefore optically thick, artificially extending the photosphere. This problem disappears rapidly as more mass expands and dynamically overwhelms the tenuous vac-

uum medium. To circumvent this problem we keep the CELMO density floor at $5 \times 10^{-10} \text{ g cm}^{-3}$. This density floor would affect the computation of the light in later phases of the expansion, where the medium has expanded sufficiently to decrease in density. However, for the optically thick, early part of the interaction considered here the exact value of the density floor has no effect on the determination of the photospheric location.

A far greater problem is that the hot vacuum warms up any outer stellar layers that are adjacent to it and which have lower density. This can clearly be seen by comparing the density and temperature panels both in Figs. 1 and 2. These outer layers are those where we seek to extract the value of the temperature and we see that even if the resolution were higher, their temperature is compromised by the hot vacuum.

3.4. Effective temperature determination from flux conservation

An alternative approach is calculating the luminosity using the radiative flux across a thin layer located behind the overheated photosphere. In Fig. 7, left panel, we show a density cut at 75 days, along a line marked in Fig. 1 (top row, middle panel). Along this line we read values of the density, opacity, and we calculated values of $\partial u_{\text{rad}}/\partial r$. Values of $\partial u_{\text{rad}}/\partial r$ across the photosphere on the left hand side of the gas distribution are plotted in Fig. 7, right panel. The red symbols in Fig. 7, right panel, are values of the gradient characterising the hot vacuum just to the left of the photosphere, while the blue symbols are values just inside the photosphere. The symbols are $3.4 R_{\odot}$ apart, the resolution of the grid. As can be seen, the cells straddling the photosphere have quite a range of values of $\partial u_{\text{rad}}/\partial r$. Just inside the photosphere the first ~ 8 -10 cells are affected by artificial heating as can be seen in the temperature panel in Fig. 2. Values of the gradient in the cells immediately behind those are $\sim 10^{-9} \text{ erg cm}^{-4}$. Values of the opacity at corresponding depth is $\sim 100 \text{ cm}^2 \text{ g}^{-1}$, while the density is $\sim 4 \times 10^{-8} \text{ g cm}^{-3}$.

In order to check on the viability of this scheme we assume that the distribution of gas is spherical and adopt

Eq. 1 with a mean radius value calculated as the radius of the sphere that has the same volume as that contained by the photosphere at that time. This is $180 R_{\odot}$ (see Fig. 10). With this radius we calculate an approximate luminosity of $\sim 1 L_{\odot}$, much lower than even the initial stellar luminosity of $648 L_{\odot}$, while we expect a value similar or larger. Aside from the uncertainty affecting the choice of the right values for gradient and opacity, the reason for this discrepancy must be related to the thermodynamic properties of the gas. At the location we sampled, the quantities reflect the convective envelope where the flux is not transported by radiation, similar to what shown in Fig. 4 for time zero. This exercise is unlikely to provide us with a meaningful value of the overall luminosity of the gas distribution even if, instead of assuming spherical symmetry we calculated the flux at that pixel, assumed that it characterises the photosphere and integrated to obtain the luminosity using the actual shape of the gas distribution.

3.5. Effective temperature determination from a stratified temperature distribution

A final attempt to resolve the problem of the determination of the effective temperature was made by calculating a stratified, one dimensional atmosphere. This atmosphere could be effectively overlaid on the gas distribution and normalised at a location inside the photosphere, where we have confidence that the values of temperature and density are not affected by the vacuum temperature. By carrying out this exercise, however, we see that the choices are arbitrary and that the eventual value of the effective temperature has a severe uncertainty.

This method assumes that the density in the outer parts of the star follows a stratification structure with the following decaying power law:

$$\rho(r) = \rho_0 \left(\frac{r_{\text{ph}}}{r} \right)^2, \quad (3)$$

where $\rho_0 = \rho(r_{\text{ph}})$ and r_{ph} is a grid point at the photosphere. Assuming that the exterior of the star behaves like an isentropic ideal gas with

$$P\rho^{-\gamma} = K, \quad (4)$$

$$P\rho^{-1} = \frac{\bar{R}}{M}T, \quad (5)$$

where P , ρ and T are the pressure, density and temperature of the fluid respectively; M and \bar{R} are the molar mass and universal gas constant, respectively and K is a constant to be defined. Once again the adiabatic index is $\gamma = 5/3$.

From Eq. 3, 4 and 5 we can derive an expression for the temperature within the outer stellar gaseous layers:

$$T = T_0 \left(\frac{r_{\text{ph}}}{r} \right)^{4/3}, \quad (6)$$

$$T_0 = \frac{MK\rho_0^{2/3}}{\bar{R}}. \quad (7)$$

In Fig. 8, left column, we plot the density profile from the simulations alongside the optical depth that is calculated using that density, the opacity tables and values of the temperature that are calculated using the two following methods. In the first method, for every ray and every

time, we used the simulation data and selected a cell just inside the photosphere, where we estimated that the value of the temperature was not affected by the hot vacuum. For this cell, we then read the temperature and position values and used these values as $\{T_0, r_{\text{ph}}\}$ in Eq. 6, thereby calculating values of T for every value of r outside the location of r_{ph} . Alternatively, a second method was to use a set of values $\{T_0^*, r_{\text{ph}}^*, \rho_0^*\}$ from the simulation at time zero to calculate K in Eq. 7 and then use that value of K to calculate the temperature at other points and other times, anchoring Eq. 6 at a point inside the photosphere at which we know the density, ρ_0 , and the coordinates, r_{ph} .

The first method (red line in Fig. 8, right column) assumes that the temperature of the simulation is accurate inside the star. However, given the high temperature vacuum, we selected only cells with a negative gradient of the temperature profile (in Fig. 8 these points are at 0.37, 0.54 and 0.79 AU). On the other hand, the second method uses the density and the value of K , which is calculated with initial data only. Therefore, in this case we assume that the density is accurate inside the star and the temperature of the atmosphere follows Eq. (3).

Finally, the values of density needed to calculate the optical depth can be taken from the data directly, or, more self consistently with the stratification method, using Eq. 3. We tested both cases. The results are similar. Therefore, in Fig. 8 we present results obtained using the numerical values of the density only.

As can be seen, the optical depth reaches a value of $2/3$ at two different locations for the two methods. At those locations, the values of the temperature can be read from the right hand side column of Fig. 8 and they are listed in Table 1. As is clear, these values vary greatly depending on the method followed, demonstrating that the values are arbitrary.

TABLE 1
EFFECTIVE TEMPERATURE AND PHOTOSPHERE LOCATION.

Time (days)	fit 1		fit 2	
	T_{eff} (K)	$r_{\tau=2/3}$ (AU)	T_{eff} (K)	$r_{\tau=2/3}$ (AU)
0	1337	4.2	1884	3.1
75	1132	4.0	6480	1.3
135	4579	3.9	6351	2.0

3.6. A provisional solution to determine the effective temperature

During our hydrodynamic simulations, the fluid starts in the optically thick regime, but as the gas expands it may become optically thin, at which point the photosphere and its temperature can be more easily determined (although in the part of the simulation presented in this paper, the fluid remains optically thick). Normally, the simulation begins with a single star model with known effective temperature and luminosity from the original 1D model. As the companion starts its infall through the primary stars' gaseous layers the optically thick photosphere expands. As long as the gas distribution remains fully optically thick and the temperature of the photosphere is ill-defined (as explained in Sec. 3.2) we make the following approximation: the first opaque

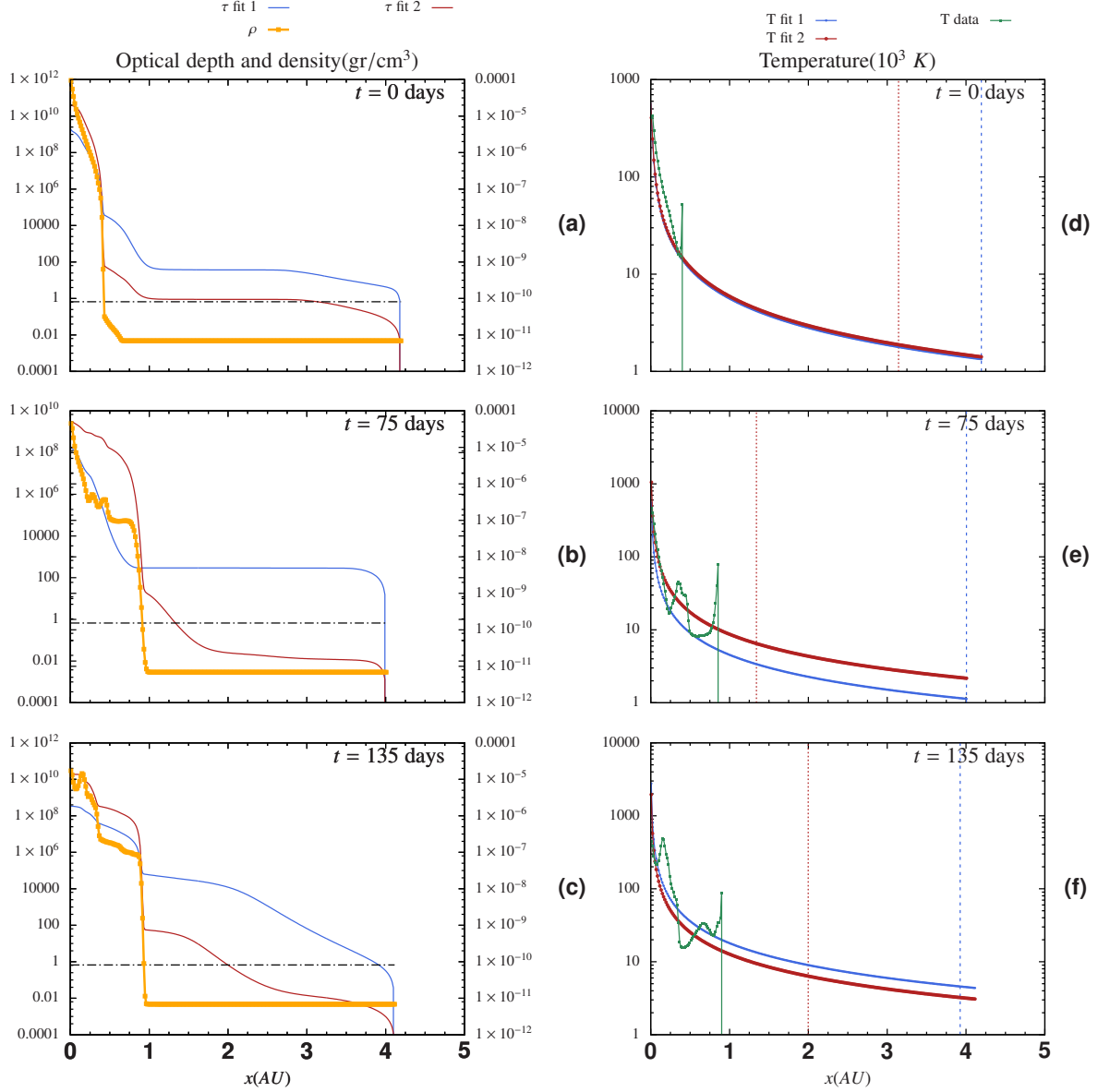


FIG. 8.— Left column: the density profile (yellow line, left vertical scale) at three times in the simulation along a ray in the $+x$ direction through the centre of the domain. Optical depths calculated using methods 1 (blue line, right vertical scale) and 2 (red line, right vertical scale) – see text. The horizontal line marks the $\tau=2/3$ level. Right column: temperature as read from the simulation (green line – the upturn at larger radii is due to heating from the hot vacuum) and temperature fits using methods 1 (blue line) and 2 (red line) – see text. The red and blue vertical lines mark the locations of the photosphere according to the two fits. The respective values of the effective temperature are listed in Table 1.

grid point is reassigned to be the $\tau = 2/3$ surface point with temperature $T = T_{\text{eff}}$, unless the temperature at the centre of the cell is lower than the effective temperature of the initial model, in which case we use the actual value:

$$T = \begin{cases} T_{\text{eff}} & \text{if } T \geq T_{\text{eff}} \\ T & \text{if } T < T_{\text{eff}} \end{cases}, \quad (8)$$

This implicitly assumes that at $t > 0$ the temperature of the expanding photosphere *decreases*, something that, as we will see in Section 5 is not always the case.

We also ensure that the combination of temperatures used does not lead to a total luminosity smaller than

the initial stellar luminosity, since the stellar luminosity is provided by a thin shell resting on the core of the primary and the CE interactions we are modelling are not thought to alter the nuclear burning rate on short timescales.

For the short time over which the photosphere remains optically thick, using a constant value of the effective temperature is likely correct to better than a factor of two, since the temperature is regulated by the opacity and there is no time for radiative cooling. However, this is still a problematic assumption and the single largest challenge in determining the light from this type of simulation. We discuss this further in Section 6.

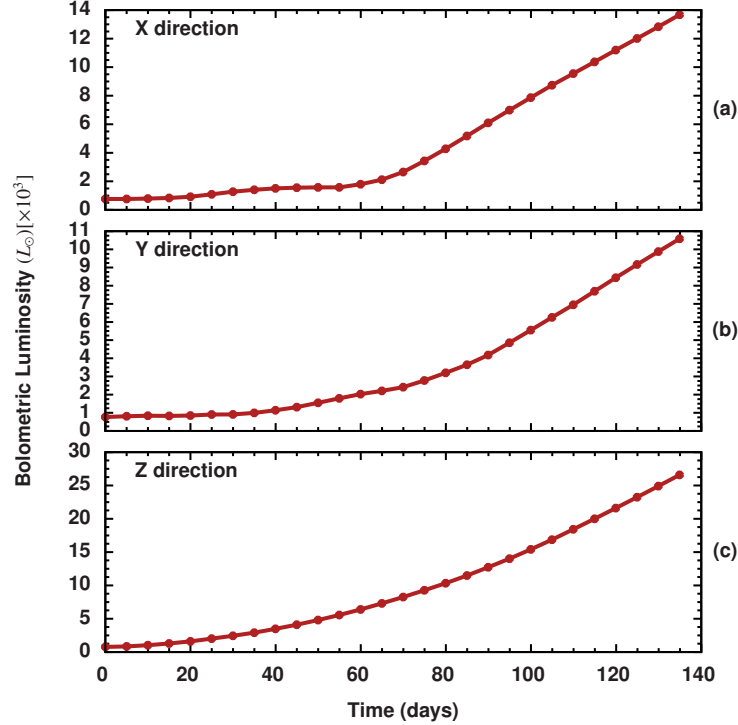


FIG. 9.— The bolometric luminosity as function of time for the highest ENZO resolution available ($N = 512$) towards each of the three directions

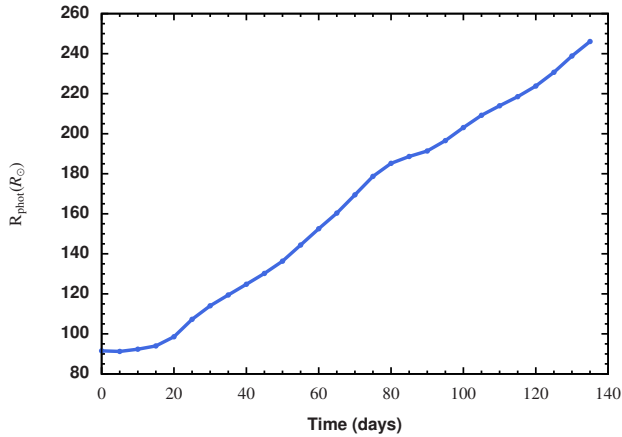


FIG. 10.— The radius of a sphere that has the same volume as the photospheric surface.

4. RESULTS: TOWARDS CALCULATING THE LIGHT CURVE OF A COMMON ENVELOPE SIMULATION

In this section we show the light curve for well studied CE evolution simulations: Enzo2 from P12, which we have carried out with a computational domain four times as large and the same resolution, as explained in Sec. 2. In Fig. 9 we show the bolometric light as seen by an observer located along three orthogonal directions, parallel to the x , y and z axes, while in Fig. 10 we show the volume-equivalent radius of the photosphere. We emphasise that the values of the temperature are almost always those of the initial T_{eff} of the star (3200 K, see Table 1 in Appendix) because the values of the photo-

sphere almost never drop below this value during the early, optically-thick photospheric expansion. This effectively means that we are assuming a constant temperature photosphere. In Fig. 11 we show density slices both on the orbital and perpendicular planes. During the entire CE evolution, the model remains effectively optically thick. In addition, as soon as stellar material leaves the domain the photosphere is effectively lost. Despite our calculation with a larger computational domain, this happens at approximately 135 days, which is short of the ~ 200 days taken by the fast in-fall phase and even shorter than the ~ 1000 days of the entire simulation run of P12.

Throughout this entire CE simulation, the photosphere coincides with the density of the CELMO density floor. However, lowering this floor further does not change the light output because of the steep density gradient at the photosphere. A very small difference might be found toward the end of the simulation time. As can be seen in Fig. 11, at 75 and 135 days, some material extends past the photosphere. This gas has a density intermediate between the ENZO and CELMO density floors and could be optically thick, thereby extending the photospheric area slightly. However, in our simulation this very low density stellar gas has a temperature that is greatly increased by the low density, high temperature vacuum medium and therefore cannot be studied.

In Fig. 12 we show the I band luminosity of one of the two perpendicular views, setting the object at 1 kpc and including no reddening. The calibration values to derive the magnitudes from the luminosities are those found in Appendix A.1. The $V - I$ colour of the initial model is 1.98 and would mostly not change over time since the photospheric temperature is effectively constant. The

initial rise of the I band luminosity is almost 3 magnitudes in 135 days.

The total radiated outburst energies between the beginning of the simulations and 135 days are 3.7×10^{43} , 3.5×10^{43} and 9.6×10^{43} erg for the x , y and z directions, respectively. We compare these energies with the total energy in the AGB star at the start of the simulation (namely its thermal, kinetic and potential energies) which is $\sim -2 \times 10^{46}$ erg. This validates the adiabatic approach for the short timescale we have simulated here.

5. GUIDANCE FROM OBSERVATIONS

5.1. Comparisons with transients

At least three transients have been credibly identified as CE interactions, primarily because their progenitors were observed: V1309 Sco (Tylenda et al. 2011), M101-OT (?), and M31-2015 LRN (MacLeod et al. 2016). Due to similar light and spectral characteristics after the outburst, other transients, such as V 838 Mon (Bond et al. 2003) or NGC4490-OT (Smith et al. 2016) have been suggested as having a similar origin. Here we carry out a comparative discussion of those aspects of the observations that today or in the near future will be the most useful to constrain CE simulations. We also highlight those aspects of the simulations that will be best constrained by observations. We concentrate on M31-2015LRN for which MacLeod et al. (2016) have extracted system parameters from their observations.

V 1309 Sco is in a way the system that is the closest to our simulations, in light of its low mass, a $\sim 1.5 M_{\odot}$ subgiant interacting and merging with a $\sim 0.15 M_{\odot}$ companion (Tylenda et al. 2011). M31-2015LRN (and likely V 838 Mon) is possibly next, in terms of system's mass: a $3 - 5.5 M_{\odot}$ primary interacted with a $0.1 - 0.6 M_{\odot}$ companion and thought to have undergone a CE merger event. M101-OT was instead thought to come from the interaction between an $18 M_{\odot}$ primary and a $1 M_{\odot}$ companion, with NGC4490-OT being even more massive, though an actual value of the mass could not be derived (Smith et al. 2016). The peak absolute luminosities of these outbursts are listed in Table 2, alongside their lightcurve behaviour.

From observations of transients, quantities such as the evolution of the photospheric radius, temperature and luminosity, as well as ejected masses, velocities and timescales of the various phases can be determined, subject to some uncertainties such as on distance and reddening. MacLeod et al. (2016) used photometry of the M31-2015LRN outburst to deduce that the photospheric radius increased between 200 and $400 R_{\odot}$ before peak brightness and then to $2000 R_{\odot}$ in the next 30 days. The photospheric expansion velocity was measured to be 360 km s^{-1} from spectroscopy. They also determined that the photospheric temperature increased between $\sim 5000 \text{ K}$ and $\sim 7000 \text{ K}$ during the rise to peak (or $\sim 6500 \text{ K}$ to $\sim 11500 \text{ K}$ for the highest possible reddening value), followed by a steady decrease to $\sim 3000 \text{ K}$ in the next 50 days. Overall, the bolometric luminosity increased between 10^{38} and $2 \times 10^{39} \text{ erg s}^{-1}$ during the rise (2×10^{38} and $7 \times 10^{39} \text{ erg s}^{-1}$ for the highest reddening value) and declined to $\sim 5 \times 10^{38} \text{ erg s}^{-1}$ in the next 50 days.

From our simulations the most reliable quantity is the

photospheric radius evolution over 135 days: the volume-equivalent radius (Fig. 10) increased between 85 and $250 R_{\odot}$, recalling that this simulated radius may not have reached its maximum extension. Subject to the caveat of the uncertain temperature (Section 3) the simulated bolometric luminosity goes from 648 to $14000 L_{\odot}$ (x -direction) in 135 days (10^{36} to $3 \times 10^{37} \text{ erg s}^{-1}$). Our progenitor's absolute magnitudes are $M_{I,\text{prog}} = -2.9$ and $M_{V,\text{prog}} = -0.9$ (using the average $V - I$ value calculated above), while at 135 days we measure $M_{I,135\text{d}} = -6.8$ and using the same color correction we obtain a value of $M_{V,135\text{d}} = -4.8$.

Lacking at present the ability for a direct comparison, we can however still place the simulated values of M_V and M_I for the progenitor and for the expanded star on the mass vs. absolute magnitude plot of Kochanek (2014), who showed that the more massive systems have brighter outbursts. As pointed out by Smith et al. (2016) this, and the fact that more massive progenitors have longer outbursts, could be explained by the fact that more massive progenitors have more kinetic energy and angular momentum and longer radiation diffusion times. Using the fits of Kochanek (2014), we would expect a $0.9 M_{\odot}$ progenitor to have $M_{V,\text{prog}} = 4.7$ and $M_{I,\text{prog}} = 3.5$. Our progenitor is brighter and redder than predicted by the fit of Kochanek (2014), likely because our star is evolved, while the fitted data are for unevolved stars. In fact OGLE-2002-BLG-360, also plotted by them, but not fitted, is a more evolved star and is indeed brighter. Their fits would predict that a $0.9 M_{\odot}$ unevolved star would have an outburst with peak brightness $M_{I,\text{peak}} = -5.3$ and $M_{V,\text{peak}} = -3.4$. Comparing their predicted I band with ours (Table 1) shows that our magnitude is at least 1.5 mag brighter, though the $V - I$ colours are similar. This is at this stage acceptable in view of the many uncertainties.

5.2. Constraints from Mira giants

The temperature of the photosphere and the luminosities are not well constrained; as explained, the temperature is effectively kept constant at the value of the progenitor's effective temperature. Mira variables are AGB giants with characteristics similar to the stars we have considered in our simulation. They expand due to pulsations on timescales similar to the expansion timescales considered here and in so doing their radius changes similarly to the radial expansion considered here. In models of α Ceti (Ireland et al. 2008, 2011), the effective temperature of the photosphere changes between 3800 K and 2200 K during half a pulsation cycle of 330 days (i.e., 165 days). During this time the radius expands by a factor of 2.3. This is similar to what was found for other Mira stars. Our calculation over 135 days sees an approximate radial expansion over a similar factor. Such a decrease in temperature would give a reduction in luminosity by a factor of ~ 10 compared to the values we have estimated.

On the other hand, the expanding photosphere may *not* initially cool. In the case of M31-2015LRN, the expanding photosphere was initially *heated* by shocks, instead of cooling adiabatically by expansion, and only later cooled. Therefore, observations caution us that assuming that the photosphere initially cools by expansion may be misguided.

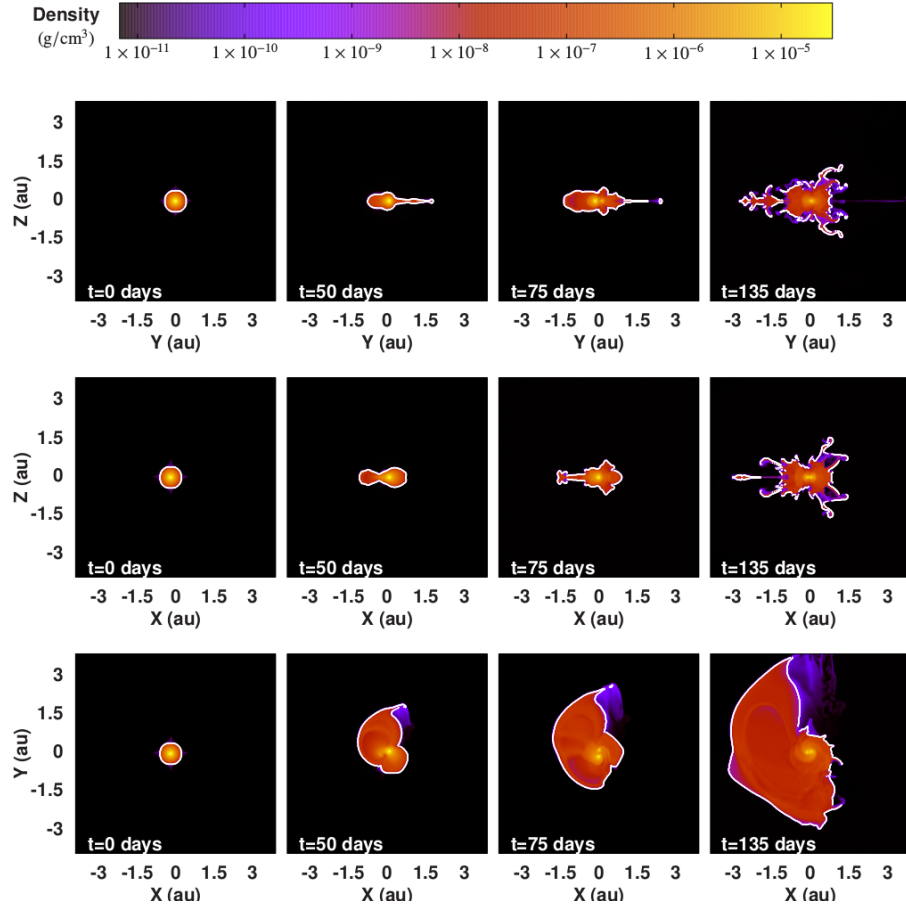


FIG. 11.— Density slices located at $X = 0$, $Y = 0$, and $Z = 0$ (from top to bottom), taken at times $t = 0$ (column 1), 50 (column 2), 75 (column 3), and 135 (column 4) days. The white line represents the photosphere as located by an observer on the same plane as the density slice.

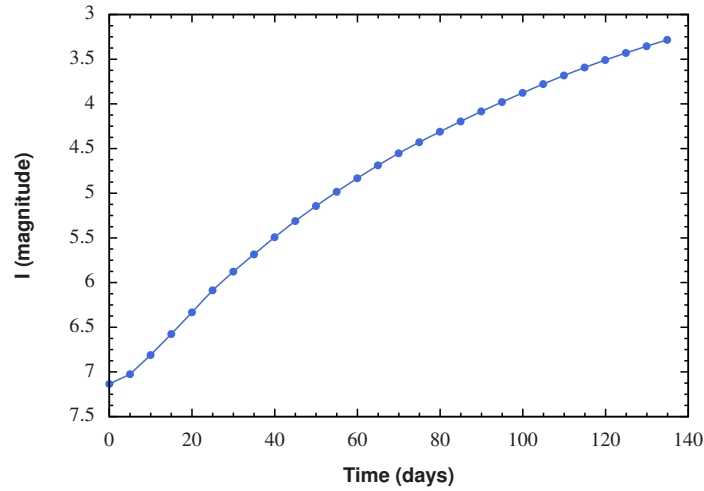


FIG. 12.— I -band magnitude of the system observed along the z direction (looking perpendicularly to the orbital plane), as if the system were observed from 1 kpc with no reddening.

Name	$M_{\text{Band}}(\text{peak})$ (mag)	Band	M_1 (M_{\odot})	M_2 (M_{\odot})	Plateau?
Simulation ¹	< -4.8 ., < -6.8	V, I	0.9	0.6	–
V 1309 Sco ²	$-6.9, -7.9$	V, I	1.5	0.15	n?
V 838 Mon ³	-9.6	V	5-10	–	n
M31-2015LRN ⁴	-9.5	V	3-5.5	0.1-0.6	y
M101-OT ⁵	-12.6^a	r	18	1	y
NGC 4490-OT ⁶	-14	unfilt.	20-30:	–	?

¹P12 and this work; “.:” means very uncertain value.²Tylenda et al. 2011;

³Bond et al. 2003; ⁴MacLeod et al. 2016; ⁵?

⁶Smith et al. 2016. ^aCould have been brighter, peak not observed.

TABLE 2
SOME CHARACTERISTICS OF OBSERVED TRANSIENTS INTERPRETED AS COMMON ENVELOPE INTERACTIONS/MERGERS.

5.3. *Recombination energy as an agent in the the common envelope ejection*

Another related issue of fundamental importance is that of recombination energy released upon recombination of hydrogen and helium. The release of recombination energy as light may explain the plateau in certain type of Type II supernovae (Ivanova et al. 2013). MacLeod et al. (2016) argue that the plateau in the light curve of the transient M31-2015LRN after the maximum is due to such energy release.

However, Ivanova et al. (2015) and Nandez & Ivanova (2016) argued that during the common envelope expansion, recombination energy is released at such high physical depth that the optical depth should also be large, making the energy released there entirely available to generate pressure that results in the expulsion of the CE. At such depth, they argued, even the dramatic decrease in opacity of recombined gas may not be sufficient to liberate the energy as light on short timescales and is therefore available to do work. This is a very important point that needs a resolution: if recombination energy does not escape, then it must be included in CE simulations, but if part or all of it escapes, then CE simulations that include recombination energy and that are run in the *adiabatic* approximation, will overestimate the ejected mass, ejecta's speeds, and produce unphysical in-spiral behaviours (see Harpaz 1998, for why expanding, recombining giants do not blow themselves apart). Observations such as those listed here, and particularly the presence or absence of a plateau in the lightcurve, may point to an observational constraint on how recombination energy is transformed in the star.

5.4. *What happens just before the common envelope in-spiral?*

Another aspect of the interaction where observations will provide us with a quantitative constraint concerns what precedes the fast in-spiral. MacLeod et al. (2016) suggested that there can be two pre-in-spiral scenarios with distinct observational characteristics. The first, which they apply to M31-2015LRN, is a fast (days) pre-in-spiral phase where a secularly stable orbit is destabilised by the Darwin instability (Darwin 1879). This leads to Roche lobe overflow and the CE in-spiral in quick succession. This phase is characterised by an early ejection of a low mass, but optically thick shell that is observed as an expanding photosphere. At the same time the photospheric temperature increases as this gas is shock-heated by the early in-spiral. This shell is ejected with speeds above escape velocity. Right after this ejection the full photosphere expands and cools, driven by orbital energy deposited during the in-spiral. The second scenario, is a slower one: after Roche lobe overflow the mass transfer remains stable and leads to an outflow from the second Lagrangian point at lower ejection speed (25% of escape speed). The expanding gas creates a wall of material into which the subsequent expansion phase, driven by the in-spiral, will collide. The difference between these two scenarios is key to understanding when a CE is avoided.

The simulation presented in P12 and this paper cannot help chose between the two scenarios because the companion is placed on the surface of the giant at the start

of the simulations and the primary therefore already well exceeds its own Roche lobe radius. However, one of the SPH simulations presented by Iaconi et al. (2017) may afford a better comparison. That simulations is identical to that of P12 analysed here, but it started with a wider orbital separation, with the primary at Roche lobe contact. The stable mass transfer phase, preceding the fast CE in-spiral, lasts a decade, but this is likely a lower limit (Reichardt 2015, and Reichardt et al., in preparation).

During this Roche lobe overflow phase, mass is ejected from the second Lagrangian point (L2, on the side of the companion) with speeds of $100\text{--}150\text{ km s}^{-1}$, which is above the local escape speed of $\sim 60\text{ km s}^{-1}$, while at the third Lagrangian point (L3, on the side of the primary), gas is being ejected with speeds of $\sim 40\text{ km s}^{-1}$, which is similar to the local escape speed of $\sim 50\text{ km s}^{-1}$. The expansion of the photosphere measured here is between 85 and 250 R_{\odot} and lasts 135 days, implying an expansion speed of 9 km s^{-1} lower than the escape speed and lower than the speed of the ejecta seen emerging from L2 and L3. Once again is it difficult to make quantitative comparisons at this time, but as these values become refined, they will be those that allow us to discriminate what happens before the CE in-spiral and how this phase affects the CE proper and the post-CE parameters.

CE interactions and merger observations assume that the expanding primary was caught in a CE right after the main sequence as the star commenced its journey towards the red giant branch. However, statistically, the rate of interactions involving more evolved giants should be larger, because there are more companions at larger separations (Duchêne & Kraus 2013). As more transients and their progenitors are observed, we will know whether the apparent overabundance of sub-giant branch mergers is due to their being particularly bright or simply to our current uncertainty on the nature of the progenitors. If the former, an explanation could be that the CEs we observe are those with a more bound envelope (more massive and compact) where the companion penetrates deeper and tends to merge more readily, releasing more energy.

5.5. *Dust formation during common envelope expansion*

Finally, observations tell us that dust will have to be considered in the calculation of the light, as it may deeply affect the lightcurve. As early as during the first few days of the expansion, dust could be produced, as seen in V 1309 Sco (Tylenda et al. 2011) that brightened over a period of approximately 5 years and then suddenly dimmed by about a magnitude (in the *I* band) just before the outburst. Nicholls et al. (2013) obtained an IR spectrum approximately a year after the optical outburst peak and determined that a substantial amount of dust must have condensed in this object, though a determination of the dust mass was impossible without knowledge of the dust geometry. This system was known to be a close-to-edge-on contact binary. We conjecture that the dust forms in a disk along the equator. This is in line with the large dust grain size measured by Nicholls et al. (2013) that necessitate a disk environment. Additionally, Chesneau et al. (2014) measured an elongated dusty environment, interpreted as a disk, in V838 Mon. We could

therefore conjecture that while dust formation during the CE in-spiral is possible, indeed likely, it may primarily influence the light as seen along the orbital plane, leaving perpendicular viewpoints relatively unobstructed.

6. SUMMARY AND FUTURE WORK

In this article, we presented a computational code to post-process the luminosity for hydrodynamic simulations. CELMO is currently designed to compute the light-curve for CE simulations performed with the ENZO code in unigrid mode. We presented a first attempt at calculating the light-curve for one of the CE simulations presented by P12, comprising an $\sim 80\text{-}R_{\odot}$, $0.88\text{-}M_{\odot}$, RGB star with a $0.6\text{-}M_{\odot}$ companion.

The computation of the light from CE interactions is paramount if we are to use current and upcoming observations to constrain simulations. Our attempt cannot at this time be considered satisfactory, because we have maintained the photospheric temperature constant over the 135 days of the simulation. With this effort we have, however, elucidated and quantified the main issues with the computation. This is a fundamental step before a solution can be determined. Below we summarise these shortcomings of the current attempt and discuss possible avenues towards a solution, some of which we will explore in future papers in this series.

The limitations of our approach can be divided into two groups. The first group includes limitations inherited from the 3D hydrodynamic computation itself, while the second group comprises physical limitations due to simplifications in the light calculation.

The main computational limitation are the impossibility to resolve the value of the photospheric temperature during the optically thick phase of the expansion, and even more importantly, the heating of the outer layers by the hot “vacuum”. These make it impossible to read a photospheric temperature value directly from the simulation. According with the values of opacity and density of our models, we would be able to properly resolve the photospheric temperature, only with a cell size smaller than $0.004\text{ }R_{\odot}$ (cf. with $3.4\text{ }R_{\odot}$ for our simulation reproducing *Enzo2* of P12). The best resolution attained to date by the simulations of Ohlmann et al. (2016) is $0.01\text{ }R_{\odot}$ at the centre of the domain. Hence, this is at the edge of our capabilities even with an adaptive mesh refinement (AMR) code, as it would require between 8 and 9 levels of AMR refinement over the large volume occupied by the photosphere. Even with higher resolution, however, the problem of the external artificial heating remains.

None of the techniques we have tried to reduce the uncertainty on the effective temperature has proven satisfactory. Aside from a massive improvement in the resolution of the original calculation, which is not within immediate reach, we are exploring a way to interface ENZO and RAGE (Gittings et al. 2008) in order to exploit the latter code radiation capabilities, while using information from the ENZO computation.

Another computational limitation is one of the largest issues with hydrodynamic computations of stars using grid codes is the finite size of the domain, which allowed us to compute the light for only 135 days of the CE simulation of P12. This problem will be greatly alleviated by using the AMR version of ENZO (Passy & Bryan 2014), which will allow us to maintain resolution with a much larger box.

Our smooth particle hydrodynamics simulations (Iaconi et al. 2017) could also be used. They do not have a hot vacuum and have no computational domain limits, but at present the resolution near the photosphere is even lower than for the grid simulations due to the low density in those regions and to the computational times that at present limit the resolution to approximately a million particles.

Once the technical issues listed above have been resolved, we will have to contend with physical ones. During the initial infall the timescale is dynamical. This is the reason why simulations of this phase can avoid the inclusion of much of the physics that would dominate over longer timescales. Radiative cooling is not expected on such short timescales (as also confirmed by the fact that the total energy radiated over the initial 75 days of the interaction is much less than the initial energy of the envelope) and the thermodynamic properties of the gas should be well represented by our adiabatic calculation. Yet, later on, we can expect cooling, gas recombination and the formation of molecules and of dust. This will alter the opacities and necessitate the treatment of radiation transport. However, we note that predicting the initial lightcurve rise may not necessitate the treatment of these processes.

7. ACKNOWLEDGMENTS

It is a pleasure to thank Juhan Frank and Mark Wardle for valuable discussions and comments on the manuscript. Peter Wood is thanked for discussions regarding the properties of Mira stars. An anonymous referee is thanked for extensive comments that helped significantly the maturity of this manuscript. Thomas Reichardt is thanked for sharing some details of his upcoming publications regarding ejection speed of mass from CE interactions. This work was supported by the Australian Research Council Future Fellowship (FT120100452) and Discovery Project (DP12013337) programmes.

This research was undertaken on the NCI National Facility in Canberra, Australia, which is supported by the Australian Commonwealth Government. This work was performed on the swinSTAR supercomputer at Swinburne University of Technology. Computations described in this work were performed using the Enzo code⁶, which is the product of a collaborative effort of scientists at many universities and national laboratories.

JCP thanks the Alexander von Humboldt-Stiftung and Norbert Langer for their support.

⁶ <http://enzo-project.org>

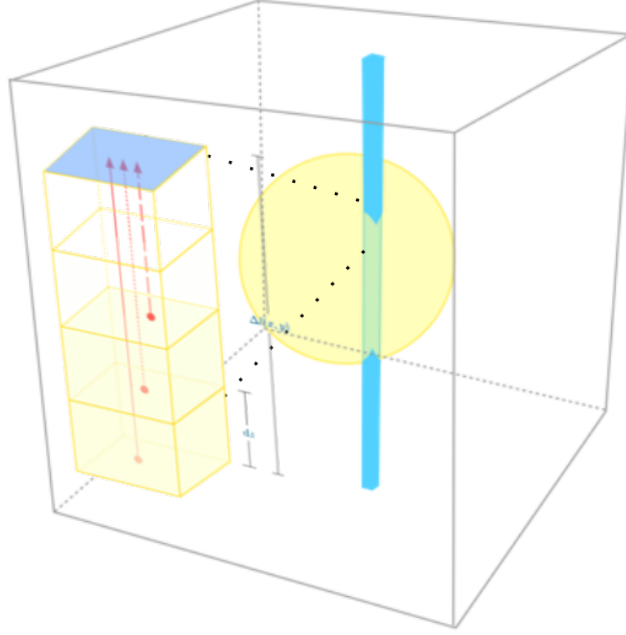


FIG. 13.— Numerical domain partition. The numerical domain is divided in columns along the line of sight. The light is computed for each volume element and the total contribution of each column integrated for each face of the numerical domain (diagram shows the case for $+Z$ propagation)

APPENDIX THE FORMULATION

Each numerical volume element, or cell, in our simulation has a temperature $T(x, y, z)$ and density $\rho(x, y, z)$. If we observe the computational domain from the positive direction of the \hat{z} axis, with the coordinate system origin in the centre of the numerical domain (see Fig. 13), we can then divide the cube into columns of area $a = \Delta x \Delta y$ and infinitesimal depth of width dz . The surface brightness of each slice is:

$$dB(\nu, \vec{r}; T) = \frac{N(\nu, z; T) h \nu}{a \omega} \frac{dz}{\Delta l(x, y)} \quad , \quad (\text{A1})$$

in units of $\text{erg s}^{-1} \text{ cm}^{-2} \text{ Hz}^{-1} \text{ sr}^{-1}$, where ω represents the solid angle subtended by the area a at the observer, and N denotes the number of photons of frequency ν emitted from the surface of area a . The energy of each photon is $h\nu$ and has an associated temperature T . The fraction $dz/\Delta l(x, y)$ denotes the proportion dz of the total length of the column $\Delta l(x, y)$ and is equal to $l(x, y)_{\text{max}} - l(x, y)_{\text{min}}$ (see Fig. 13). The specific intensity:

$$I(\nu; T) = \frac{N'(\nu; T) h \nu}{A \Omega} \quad , \quad (\text{A2})$$

(with the same units as Equation A1), is the number of photons N' with energy $h\nu$ detected at a surface of area A arriving from solid angle Ω . The number of photons arriving at the detection surface is related to the number of photons emitted by:

$$N'(\nu) = \int_{l_{\text{min}}}^{l_{\text{max}}} N(\nu, z) e^{-\tau} dz \quad , \quad (\text{A3})$$

where:

$$\tau := \int_z^{l_{\text{max}}} \kappa(x, y, \xi) \rho(x, y, \xi) d\xi \quad , \quad (\text{A4})$$

where κ and ρ are the opacity and density of the medium, respectively, and τ is the optical depth. The exponential factor takes into account the dispersion of photons between z and the surface of the volume l_{max} . The integration in z gives us the total contribution of the column.

Assuming blackbody radiation, the surface brightness of one slice in our domain is:

$$B^*(\nu; T)_{ijk} = 2 \frac{h\nu^3}{c^2} \frac{1}{e^{h\nu/kT_{ijk}} - 1} \quad (\text{A5})$$

where i, j, k are the x, y, z discrete indices of the numerical domain. The specific intensity in the respective column is:

$$I(\nu; T)_{ij} = \sum_k B^*(\nu; T)_{ijk} e^{-\int_{z_{ijk}}^{l_{\max}} \kappa(\xi) \rho(\xi) d\xi} \quad (\text{A6})$$

The radiation flux crossing the detection surface is given by:

$$S(\nu; T)_{ij} = \int_0^{2\pi} \int_0^{\pi/2} I(\nu; T)_{ij} \cos \theta \sin \theta d\theta d\phi \quad (\text{A7})$$

$$= \pi I(\nu; T)_{ij}, \quad (\text{A8})$$

where we have assumed that the observation distance $z_{\text{obs}} \gg \max(\Delta l(x, y))$ and isotropic emission of each column. The flux density \mathcal{F} is given by:

$$\mathcal{F}_{ij} = \int f(\nu) S(\nu)_{ij} d\nu, \quad (\text{A9})$$

in units of $\text{erg s}^{-1} \text{ cm}^{-2}$ where $f(\nu)$ represents a filter (see Sec. A.1). The luminosity is therefore:

$$L = \sum_i \sum_j \mathcal{F}_{ij} \Delta x \Delta y. \quad (\text{A10})$$

Convolution with filter band passes

Light curve observations are performed in specific spectral bands.

Assuming homogeneous emission in all frequencies, each volume element should radiate in the full spectrum. Therefore, we can convolve the brightness of each slice with the filter function. The energy flux density is:

$$\mathcal{F}_{\text{filt}}(T) = 2\pi \frac{k^4 T^4}{c^3 h^3} \int_0^\infty \frac{f(\chi) \chi^3}{e^\chi - 1} d\chi \quad (\text{A11})$$

$$= \frac{15\sigma}{\pi^5} T^4 \int_0^\infty \frac{f(\chi) \chi^3}{e^\chi - 1} d\chi, \quad (\text{A12})$$

where $\chi = h\nu/kT$, and h, k, c are the Planck constant, the Boltzmann constant and the speed of light, respectively.

The bolometric flux density is recovered if $f(\chi) = 1$, or:

$$\mathcal{F}_{\text{bol}}(T) = \sigma T^4. \quad (\text{A13})$$

For a star with effective temperature T_{eff} , the bolometric luminosity is $L_{\text{bol}} = 4\pi R_{\text{star}}^2 \sigma T_{\text{eff}}^4$. The effect of the filter is encoded in the factor

$$f_{\text{filt}}(T) = \frac{15}{\pi^5} \int_0^\infty \frac{f(\chi; T) \chi^3}{e^\chi - 1} d\chi. \quad (\text{A14})$$

Therefore, the energy flux density $\mathcal{F}_{\text{filt}}(T)$ takes the form

$$\mathcal{F}_{\text{filt}}(T) = \mathcal{F}_{\text{bol}}(T) f_{\text{filt}}(T). \quad (\text{A15})$$

We integrate numerically Equation (A14) using the SciPy⁷ routine of Simpson's rule. To compute the magnitude, we use the bolometric magnitude, V -band magnitude and $V - I$ colour of the Sun, $M_{\odot, \text{bol}} = 4.75$, $V_{\odot} = -26.74$ ⁸ and $(V - I)_{\odot} = 0.701$ (Ramírez et al. 2012), respectively. Additionally, we use our filters to compute the solar luminosity in the I and V bands using a blackbody curve with $T_{\text{eff}, \odot} = 5778 \text{ K}$.

⁷ www.scipy.org

⁸ nssdc.gsfc.nasa.gov/planetary/factsheet/sunfact.html

Numerical implementation

CELMO is written as a set of python classes. We use the SCIPY library for integration and interpolation and NUMPY for general mathematical operations. The purpose of the classes in CELMO are the interpolation of the opacity, the convolution of the luminosity with filter functions and the main calculation of the luminosity described in the previous section. Additionally, we use a set of Python scripts to post-process the data. CELMO uses YT (?) interface to read data from ENZO.

We use the VTK (?) data format for 3D output and ASCII format for 1D and some of the 2D quantities. CELMO requires the density field and either the temperature or the internal energy (see § 3.1). Additionally, it is necessary to specify the effective temperature of the initial model T_{eff}^0 . The output fields are: the opacity κ , the optical depth in six directions ($\pm x, \pm y, \pm z$), the specific intensity, the energy flux density in each direction, the luminosity in each direction and the volume inside the $\tau = 2/3$ surface.

We use MPI4PY (?) to take advantage of multi-core processors. It is straightforward to calculate the luminosity in a distributed computation scheme since the necessary quantities are located independently in the fluid columns.

APPENDIX

CODE VERIFICATION

In this appendix we use two simple models which are suitable for comparison with analytic expressions. The easiest case is for a fluid with constant opacity and density.

Test I. Rectangular cuboid under optically thin conditions

Fig. 14 shows a test case for an optically thin fluid. The location of the $\tau = 2/3$ surface is well resolved for the test combination of opacity, density and grid size. Similarly, the extinction factor has a smooth transition between the transparent region ($e^{-\tau} = 1$) and the opaque one ($e^{-\tau} = 0$). On the other hand, Fig. 15 shows the numerical solution for an optically thick fluid (see Section A.0.3). The only difference between these two tests is the scale of the y-axis. In the latter case the $\tau = 2/3$ surface is not properly resolved (although the plot looks similar, the y-scale is six orders of magnitude larger). The exponential factor for the optically thick case is a step function: the fluid goes from transparent to opaque from one grid point to the next.

Let us consider a cuboid $\Delta x \times \Delta y \times \Delta z$ with a fluid at constant temperature T_0 , density ρ_0 and opacity κ_0 . The specific intensity in the z direction is:

$$I(\nu; T_0) = \frac{1}{\Delta l(x, y)} \int_{-\Delta z/2}^{\Delta z/2} B^* e^{-\kappa_0 \rho_0 (\Delta z/2 - z)} dz \quad (\text{A1})$$

$$= \frac{B^*}{\rho_0 \kappa_0 \Delta z} (1 - e^{-\kappa_0 \rho_0 \Delta z}), \quad (\text{A2})$$

where Δl is the total length of the domain and B^* is the surface brightness. The flux density then is:

$$\mathcal{F}(x, y) = \frac{\sigma T_0^4}{\rho_0 \kappa_0 \Delta z} (1 - e^{-\kappa_0 \rho_0 \Delta z}), \quad (\text{A3})$$

and the luminosity in the z direction is:

$$L_z = \Delta x \Delta y \frac{\sigma T_0^4}{\rho_0 \kappa_0 \Delta z} (1 - e^{-\kappa_0 \rho_0 \Delta z}). \quad (\text{A4})$$

Similarly, we obtain the luminosity for the x and y directions.

Using the following parameters:

$$\kappa_0 = 0.3341 \text{ cm}^2/\text{gr}, \quad (\text{A5})$$

$$\rho_0 = 10^{-4} \text{ gr/cm}^3, \quad (\text{A6})$$

$$T_0 = 10^7 \text{ K}, \quad (\text{A7})$$

$$\Delta x = 3 \times 10^5 \text{ cm}, \quad (\text{A8})$$

$$\Delta y = 4 \times 10^5 \text{ cm}, \quad (\text{A9})$$

$$\Delta z = 5 \times 10^5 \text{ cm}, \quad (\text{A10})$$

we compare the analytic and numerical results. We have already shown in Fig. 14 the optical depth and the extinction factor together with the analytical curves. Fig. 16-(a) shows the relative error in the luminosity as function of resolution for three observation directions. Note that, since the size of the cuboid is different in each direction, the corresponding luminosity changes depending on the direction. We employed $1/N$ as convergence parameter which is proportional to the characteristic grid resolution h . The plot shows a linear dependency $\mathcal{O}(h)$ convergence. The relative error in the luminosity is smaller than 1.6% for each grid size.

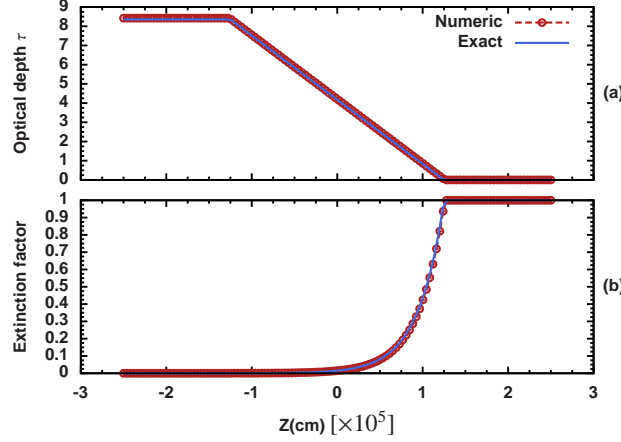


FIG. 14.— Optically thin fluid test (see Sec. A.0.1). The upper panel (a) shows a comparison between numerical and exact solutions for the optical depth in the z direction crossing the origin. The detection surface (observed) is located at $Z = 2.5 \times 10^5$ cm. The difference is not noticeable in this plot. The lower panel (b) shows the corresponding extinction factor.

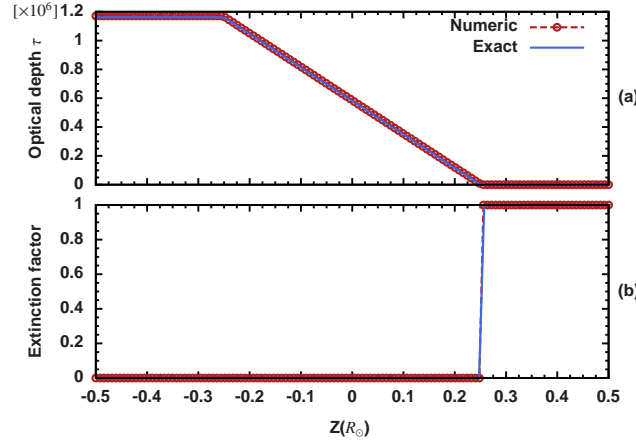


FIG. 15.— Optically thick fluid test (see Sec. A.0.3). Similar to Fig. 14, the upper panel (a) shows a comparison between numerical and exact solutions for the optical depth in the z direction crossing the origin. The detection surface is located at $z = 0.5 R_\odot$. The difference is not noticeable in this plot. The lower panel (b) shows the corresponding extinction factor.

Test II. A sphere under optically thin conditions

In the case of the cuboid the flux density does not depend on the normal coordinates. However, that is not the case for a sphere. Let's consider a static sphere of radius R_0 , temperature T_0 , constant opacity κ_0 and constant density ρ_0 . Considering a volume element in cylindrical coordinates. The parametric equation of a sphere in cylindric coordinates $\{r, \theta, z\}$ is:

$$\vec{r} = r [\cos(\theta)\hat{x} + \sin(\theta)\hat{y}] + z\hat{z}, \quad (\text{A11})$$

$$0 \leq r \leq \sqrt{R^2 - z^2} \quad |z| \leq R. \quad (\text{A12})$$

Where R is the radius of the sphere. The specific intensity in z direction is

$$I(\nu, r; T_0) = \frac{B^*}{2\sqrt{R^2 - r^2}} \int_{-\sqrt{R^2 - r^2}}^{\sqrt{R^2 - r^2}} e^{-\kappa_0 \rho_0 (\sqrt{R^2 - r^2} - z)} dz \quad (\text{A13})$$

$$= \frac{B_{\text{pk}}}{2\rho_0 \kappa_0 \sqrt{R^2 - r^2}} (1 - e^{-2\kappa_0 \rho_0 \sqrt{R^2 - r^2}}), \quad (\text{A14})$$

the flux density is

$$\mathcal{F}(x, y) = \frac{\sigma T_0^4}{2\rho_0 \kappa_0 \sqrt{R^2 - r^2}} (1 - e^{-2\kappa_0 \rho_0 \sqrt{R^2 - r^2}}), \quad (\text{A15})$$

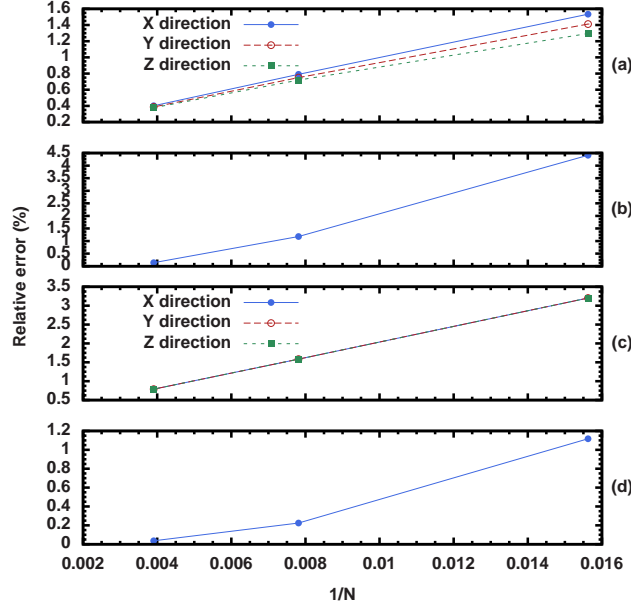


FIG. 16.— Convergence test. Relative error in the luminosity $|L - L_N|/L$ as function of $1/N$ for grid size $N \in \{64, 128, 256\}$ (notice that in every test $1/N$ is proportional to the characteristic grid resolution h). Panel (a) shows the convergence for test I, panel (b) shows the convergence for test II, panel (c) shows the convergence for test III and panel (d) shows the convergence for test IV.

and the luminosity is

$$L = 2\pi \frac{\sigma T_0^4}{\rho_0 \kappa_0} \int_0^R \frac{1 - e^{-2\kappa_0 \rho_0 \sqrt{R^2 - r^2}}}{2\sqrt{R^2 - r^2}} r dr, \quad (\text{A16})$$

$$= \pi \sigma T_0^4 \frac{e^{-2\kappa_0 \rho_0 R} + 2\kappa_0 \rho_0 R - 1}{2\kappa_0^2 \rho_0^2}. \quad (\text{A17})$$

Using the same parameters as above and $R_0 = 1.25 \times 10^5$ cm, we compare the analytic and numerical results (Fig. 16-(b)). We observe a good correspondence between the numerical result and the analytic one. In this case, the relative error is smaller than 4.5%

Test III. Rectangular cuboid under optically thick conditions

The difference between the test presented here and in Secs. A.0.4 and A.0.5 is the physical scale. A change in the scale induces a situation where the photosphere is not resolved and requires an approximation in order to overcome this lack of resolution.

This test is similar to the one presented in § A.0.1. The only change is the size of the box, which is now $\Delta x = 2 R_\odot$, $\Delta y = 1 R_\odot$ and $\Delta z = 0.5 R_\odot$. For an optically thick cuboid the luminosity in the z direction is

$$L_z = \Delta x \Delta y \sigma T_0^4 \quad (\text{A18})$$

Similarly, we obtain the luminosity for x and y directions.

Fig. 15 shows the optical depth and the extinction factor together with the analytical curves. The convergence is presented in Fig. 16-(c). Note that in this case the error depends exclusively on the grid size, independently of the direction. However, the relative errors are larger when comparing to Test I. In particular, the relative error is in the range [0.5%, 3.5%].

Test IV. A sphere under optically thick conditions

This is the equivalent to test II (Sec. A.0.2), but with a much larger size of the sphere: $R_0 = 0.25 R_\odot$. The luminosity radiated by half a solid sphere of constant temperature T_0 and radius R_0 is $L = 2\pi R_0^2 \sigma T_0^4$. Fig. 16-(d) shows the corresponding convergence test. The convergence in this case deviates from linear convergence. The relative errors are the smallest when comparing with the previous test. In Section A.0.5 we will show that for this case the error depends quadratically on the grid resolution.

Stellar models

Although it is possible to compute the luminosity for an arbitrary fluid distribution, CELMO is designed to work with hydrodynamic evolution of stars. Here we compute the luminosity of two stars calculated by the 1D code MESA and mapped into ENZO using 128^3 and 256^3 cell resolutions.

TABLE 3
PARAMETERS OF TWO MESA MODELS AND THE LUMINOSITY COMPUTED IN CELMO (L_{CELMO}) FOR TWO RESOLUTIONS. THE MEASUREMENT UNCERTAINTY IN THE LUMINOSITY IS ESTIMATED USING EQUATION (A20).

profile	R (R_{\odot})	T_{eff} (K)	L (L_{\odot})	L_{CELMO} (L_{\odot})	
				128^3	256^3
RGB	83	3200	648	662 ± 94	638 ± 46
AGB	170	3042	2207	2202 ± 154	2204 ± 76

We use two MESA profiles in order to test the computation of the initial luminosity, a smaller red-giant-branch (RGB) star and a larger asymptotic-giant-branch (AGB) star whose parameters are listed in Table 3. Both of these stars are in the optically thick regime. Therefore, the results are similar to the optically thick solid sphere (Sec. A.0.4). The stars cover most of the numerical domain. In Table 3 we see how the error is reduced with increasing resolution. This serves as an additional verification tests and gives a measure of the uncertainty on the luminosity when there is no uncertainty in temperature. This is effectively dominated by locating the photosphere which is in turn is uncertain by at most a resolution element.

The approximate error in the calculation of the luminosity is given by the errors on the temperature (ΔT) and on the radius (ΔR_*):

$$\Delta L = \frac{\partial L}{\partial R} \Delta R + \frac{\partial L}{\partial T} \Delta T \quad (\text{A19})$$

For a star of radius R_* , effective temperature T_{eff} and luminosity $L_* = 4\pi\sigma R_*^2 T_{\text{eff}}^4$, the relative error is:

$$\frac{\Delta L_*}{L_*} = 2 \frac{\Delta R}{R_*} + 4 \frac{\Delta T}{T_{\text{eff}}} \quad (\text{A20})$$

For a numeric grid with Δx , Δy and Δz , the radius R_{phot} of our initial model is located in a cell defined by (x_i, y_j, z_k) and $(x_{i+1}, y_{j+1}, z_{k+1})$. Therefore, the difference between the radius of the star and the numerical one is $\Delta R = |R_* - R_{ijk}|$ and satisfy the inequality $\Delta R \leq \sqrt{(\Delta x)^2 + (\Delta y)^2 + (\Delta z)^2}$. On the other hand, the $\Delta T = 0$ since we initially assign the effective temperature T_{eff} to the grid points in the photosphere. The estimation of the errors in Table 3 are calculated under these assumptions.

REFERENCES

- Alexander D. R., Ferguson J. W., 1994, *ApJ*, 437, 879
- Bond H. E., Henden A., Levay Z. G., Panagia N., Sparks W. B., Starrfield S., Wagner R. M., Corradi R. L. M., Munari U., 2003, *Nature*, 422, 405
- Chesneau O., Millour F., De Marco O., Bright S. N., Spang A., Banerjee D. P. K., Ashok N. M., Kamiński T., Wisniewski J. P., Meilland A., Lagadec E., 2014, *A&A*, 569, L3
- Darwin G. H., 1879, *The Observatory*, 3, 79
- De Marco O., Izzard R. G., 2017, *PASA*, 34, e001
- De Marco O., Passy J.-C., Moe M., Herwig F., Mac Low M.-M., Paxton B., 2011, *MNRAS*, 411, 2277
- Dominik M., Belczynski K., Fryer C., Holz D. E., Berti E., Bulik T., Mandel I., O’Shaughnessy R., 2012, *ApJ*, 759, 52
- Dominik M., Berti E., O’Shaughnessy R., Mandel I., Belczynski K., Fryer C., Holz D. E., Bulik T., Pannarale F., 2015, *ApJ*, 806, 263
- Duchêne G., Kraus A., 2013, *ARA&A*, 51, 269
- Gittings M., Weaver R., Clover M., Betlach T., Byrne N., Coker R., Dendy E., Hueckstaedt R., New K., Oakes W. R., Ranta D., Stefan R., 2008, *Computational Science and Discovery*, 1, 015005
- Grevesse N., Noels A., 1993, *Physica Scripta Volume T*, 47, 133
- Grevesse N., Sauval A. J., 1998, *Space Sci. Rev.*, 85, 161
- Harpaz A., 1998, *ApJ*, 498, 293
- Iaconi R., Reichardt T., Staff J., De Marco O., Passy J.-C., Price D., Wurster J., Herwig F., 2017, *MNRAS*, 464, 4028
- Ireland M. J., Scholz M., Wood P. R., 2008, *MNRAS*, 391, 1994
- Ireland M. J., Scholz M., Wood P. R., 2011, *MNRAS*, 418, 114
- Ivanova N., Justham S., Avendano Nandez J. L., Lombardi J. C., 2013, *Science*, 339, 433
- Ivanova N., Justham S., Podsiadlowski P., 2015, *MNRAS*, 447, 2181
- Ivanova N., Nandez J. L. A., 2016, *MNRAS*, 462, 362
- Kashi A., Soker N., Moskovitz N., 2013, *MNRAS*, 436, 2484
- Kasliwal M. M., 2012, *PASA*, 29, 482
- Kochanek C. S., 2014, *ApJ*, 785, 28
- Kulkarni S. R., Ofek E. O., Rau A., Cenko S. B., Soderberg A. M., Fox D. B., Gal-Yam A., Capak P. L., Moon D. S., Li W., Filippenko A. V., Egami E., Kartaltepe J., Sanders D. B., 2007, *Nature*, 447, 458
- Kuruwita R. L., Staff J., De Marco O., 2016, *MNRAS*, 461, 486
- MacLeod M., Macias P., Ramirez-Ruiz E., Grindlay J., Batta A., Montes G., 2016, *ArXiv e-prints*
- Martini P., Wagner R. M., Tomaney A., Rich R. M., della Valle M., Hauschildt P. H., 1999, *AJ*, 118, 1034
- Mitalas R., Sills K. R., 1992, *ApJ*, 401, 759
- Mould J., Cohen J., Graham J. R., Hamilton D., Matthews K., Picard A., Reid N., Schmidt M., Soifer T., Wilson C., Rich R. M., Gunn J., 1990, *ApJ*, 353, L35
- Nandez J. L. A., Ivanova N., 2016, *MNRAS*, 460, 3992
- Nandez J. L. A., Ivanova N., Lombardi Jr J., 2013, *ArXiv e-prints*
- Nandez J. L. A., Ivanova N., Lombardi J. C., 2015, *MNRAS*, 450, L39
- Nicholls C. P., Melis C., Soszyński I., Udalski A., Szymański M. K., Kubiak M., Pietrzyński G., Poleski R., Ulaczyk K., Wyrzykowski L., Kozłowski S., Pietrukowicz P., 2013, *MNRAS*, 431, L33
- Ohlmann S. T., Röpké F. K., Pakmor R., Springel V., 2016, *ApJ*, 816, L9
- Ohlmann S. T., Röpké F. K., Pakmor R., Springel V., Müller E., 2016, *MNRAS*, 462, L121
- Passy J.-C., Bryan G. L., 2014, *ApJS*, 215, 8
- Passy J.-C., De Marco O., Fryer C. L., Herwig F., Diehl S., Oishi J. S., Mac Low M.-M., Bryan G. L., Rockefeller G., 2012, *ApJ*, 744, 52
- Pejcha O., Metzger B. D., Tomida K., 2016a, *MNRAS*, 461, 2527
- Pejcha O., Metzger B. D., Tomida K., 2016b, *MNRAS*, 455, 4351
- Politano M., van der Sluys M., Taam R. E., Willems B., 2010, *ApJ*, 720, 1752
- Politano M., Weiler K. P., 2007, *ApJ*, 665, 663
- Ramírez I., Michel R., Sefako R., Tucci Maia M., Schuster W. J., van Wyk F., Meléndez J., Casagrande L., Castilho B. V., 2012, *ApJ*, 752, 5
- Rasio F. A., Tout C. A., Lubow S. H., Livio M., 1996, *ApJ*, 470, 1187
- Reichardt T., 2015, *M.Sc. Thesis; Macquarie University*
- Ricker P. M., Taam R. E., 2012, *ApJ*, 746, 74
- Sandquist E. L., Taam R. E., Chen X., Bodenheimer P., Burkert A., 1998, *ApJ*, 500, 909
- Schreiber M. R., Gänsicke B. T., 2003, *A&A*, 406, 305
- Smith N., Andrews J. E., Van Dyk S. D., Mauerhan J. C., Kasliwal M. M., Bond H. E., Filippenko A. V., Clubb K. I., Graham M. L., Perley D. A., Jencson J., Bally J., Ubeda L., Sabbi E., 2016, *MNRAS*, 458, 950
- Staff J. E., De Marco O., Macdonald D., Galaviz P., Passy J.-C., Iaconi R., Low M.-M. M., 2016, *MNRAS*, 455, 3511
- Tylenda R., Hajduk M., Kamiński T., Udalski A., Soszyński I., Szymański M. K., Kubiak M., Pietrzyński G., Poleski R., Wyrzykowski L., Ulaczyk K., 2011, *A&A*, 528, A114
- Zorotovic M., Schreiber M. R., Gänsicke B. T., Nebot Gómez-Morán A., 2010, *A&A*, 520, A86+